isvr Institute of Sound and Vibration Research

Interactions Between Multiple Moving Wheels and a Railway Track

X. Sheng, D.J. Thompson and C.J.C. Jones

ISVR Technical Memorandum No 930

March 2004

University of Southampton

SCIENTIFIC PUBLICATIONS BY THE ISVR

Technical Reports are published to promote timely dissemination of research results by ISVR personnel. This medium permits more detailed presentation than is usually acceptable for scientific journals. Responsibility for both the content and any opinions expressed rests entirely with the author(s).

Technical Memoranda are produced to enable the early or preliminary release of information by ISVR personnel where such release is deemed to the appropriate. Information contained in these memoranda may be incomplete, or form part of a continuing programme; this should be borne in mind when using or quoting from these documents.

Contract Reports are produced to record the results of scientific work carried out for sponsors, under contract. The ISVR treats these reports as confidential to sponsors and does not make them available for general circulation. Individual sponsors may, however, authorize subsequent release of the material.

UNIVERSITY OF SOUTHAMPTON

INSTITUTE OF SOUND AND VIBRATION RESEARCH

DYNAMICS GROUP

Interactions Between Multiple Moving Wheels and a Railway Track

by

X. Sheng, D.J. Thompson and C.J.C. Jones

ISVR Technical Memorandum No: 930

March 2004

Authorised for issue by
Professor M.J. Brennan
Group Chairman

INTERACTIONS BETWEEN MULTIPLE MOVING WHEELS AND A RAILWAY TRACK

X Sheng, D J Thompson and C J C Jones

ABSTRACT

In this paper an approach is presented for the wheel/rail interactions generated by multiple wheels moving along a railway track which is an infinitely long periodic structure. This 'moving wheel approach' utilises the wavenumber-based method of calculation for the response of a periodic structure to a moving harmonic load. It can be applied not only to calculate the wheel/rail forces and other quantities generated by rail roughness, but also to evaluate the response due to the parametric excitation of the moving wheels. Investigations are carried out into the effects of the wheel speed, the wavelength of rail roughness and interactions between multiple wheels. The parametric excitation is realised by assuming a smooth railhead surface, and subsequently roughness equivalent to the parametric excitation is defined. This equivalent roughness may, in addition to the actual rail roughness, be input into the 'moving roughness model' and other models in which the parametric excitation has been excluded, so that the predictions from these models can be improved.

CONTENTS

1. INTRODUCTION

Wheel/rail interaction plays a key role in the generation of wheel/rail noise, the growth of rail roughness and the formation of rail corrugation. The most comprehensive and widely used wheel/rail noise generation models are those developed by Remington [1, 2] and Thompson [3, 4], with a validated standard deviation of up to 5 dB, in third-octave bands. For short-pitch rail corrugation, the model developed by Müller [5], see also [6], following studies by Valdivia [7], Hempelmann [8] and Frederick [9], is most recognised [10], although experimental validation of the model is still required. Improvements to these models have been made by many other researchers. For example, Wu [11] demonstrates the importance of including multiple wheels rather than a single one in the analysis. In order to analyse in the frequency domain, the motion of the wheels is replaced by the motion of a roughness strip in all the aforementioned and many other models. Therefore these models may be termed 'moving-roughness models' and they are linear, time invariant and with the roughness being the only excitation mechanism.

In the real situation, the wheels are travelling along the track and the roughness is stationary. Not only the irregular profile of the railhead produces dynamic wheel/rail forces, but the varying stiffness of the track due to the discrete supports also contributes to the wheel/rail dynamic interactions. In other words, vibrations are still generated in the wheel/track system even if the wheels move over a perfectly smooth rail. The excitation mechanism producing these vibrations is often termed *parametric excitation*, to distinguish it from the roughness excitation. To achieve further understanding of the mechanisms of wheel/rail noise generation, Nordborg [12] conducted a study on wheel/rail noise generation due to nonlinear effects in the contact patch and to the parametric excitation. In this study, only a single wheel was considered as a rigid body, and the rail was modelled as an Euler beam, discretely supported by dynamic systems each consisting of a railpad, a sleeper and ballast. Approaches were developed in both the time domain and the frequency domain. The time-domain approach is based on the time-domain Green's function of the track, which is calculated from the frequency-domain Green's function of the track using the fast Fourier transform technique. The time-domain approach can account for non-linearity in the wheel/rail contact, although the track itself must be a linear system. The frequency-domain approach is based on the model of 'a mass on a time-varying spring'. Here the mass represents the wheel and the time-varying spring represents the track which provides varying stiffness as the wheel passes over a sleeper bay. This idea is valuable. However in the calculation of the varying stiffness of the track, the author sets $x = ct$ (where c is the speed of the moving wheel) in the receptance, $\alpha_p(x,\omega)$, of the rail at the loading point, x, due to a unit *stationary* harmonic load of frequency ω, and then inverts the receptance to give the time-dependent stiffness of the track. It has

been shown in reference [13] that, observed in a reference frame moving with the load, the ratio (termed *the quasi-receptance*) of the displacement of the loading point to the moving harmonic load is *not* equal to $\alpha_p(x,\omega)$ with x being substituted by ct. The quasi-receptances (direct and cross) are periodic functions of time t with period equal to the sleeper-passing time. The Fourier coefficients of these periodic functions have been expressed explicitly in reference [13] in terms of an integral over the wavenumber in the longitudinal direction. Therefore the method developed in reference [13] is wavenumber-based.

In this report, this wavenumber-based method is utilised to formulate the interactions between multiple moving wheels and a railway track, rendering a new approach to the wheel/rail interaction problem. This 'moving wheel approach' can be applied not only to calculate the wheel/rail forces and other quantities generated by rail roughness, but also to evaluate the response to the parametric excitation of the moving wheels. The parametric excitation is realised by assuming a smooth railhead surface, and subsequently the roughness equivalent to the parametric excitation is defined. Detailed derivations are presented in Section 2. Results produced using this approach are presented in Section 3, firstly for a single locomotive wheel and then for four such wheels running over a conventional ballasted track at different speeds and excitation frequencies. From these results conclusions are drawn and summarised in Section 4.

2. FORMULATIONS

2.1 THE IRREGULAR VERTICAL PROFILE OF THE RAIL

Since the wavelengths of the irregularities of the railhead considered here are much shorter than the sleeper spacing, the irregularities can be assumed to be spatially periodic with a period equal to the sleeper spacing, L. The profile, denoted by $z(x)$, can therefore be expressed as a sum of an infinite number of spatial harmonics,

$$z(x) = \sum_{k=-\infty}^{\infty} Z_k e^{ik\beta_0 x} \tag{1}$$

where, $i = \sqrt{-1}$, $\beta_0 = \frac{2\pi}{L}$, $k = 0, \pm 1, \pm 2, \cdots$, Z_k is a complex number with $Z_0 = 0$. Due to the filtering effect of the wheel/rail contact patch, only roughness with wavelengths greater than about 0.02 m is important. Therefore the highest order of the harmonics that should be considered is determined by $|k| \leq \frac{2\pi}{0.02\beta_0} = 30$ if $L = 0.6$ m. Since $z(x)$ must be a real function of x, Z_{-k} must be the conjugate of Z_k.

2.2 THE INTERACTION FORCE BETWEEN A WHEEL AND THE RAIL

The track is idealised by a periodically supported rail. Since the rail is periodically supported and the roughness of the rail is assumed to be periodic in space with the period equal to the sleeper spacing, the *compressive force*, $P_l(t)$, between the lth wheel and the rail must be a periodic function of time t with period equal to the sleeper-passing time L/c, where c is the wheel speed. Thus it can be expressed as

$$P_l(t) = \sum_{j=-\infty}^{\infty} P_{lj} e^{ij\Omega_0 t} \tag{2}$$

where $\Omega_0 = \frac{2\pi c}{L} = \beta_0 c$ and P_{lj} is the amplitude of the jth harmonic component of the lth wheel/rail force. Note that, P_{l0}, or denoted alternatively by W_l, is equal to half the lth axle load, and $P_{l,-j}$ must be the conjugate of P_{lj}.

2.3 VERTICAL DISPLACEMENTS OF THE WHEELS

A wheel experiences rigid motion as well as elastic deformation. The basic rigid motion is a rotation at angular velocity Ω about the axis (z-axis) of the undeformed wheel. Observed from itself, the wheel is excited by a force with the point of action rotating around its periphery. Figure 1 shows the elastic displacements in a cylindrical coordinate system fixed on the wheel. The force is assumed to be harmonic at frequency ω, denoted by the vector $\mathbf{P}e^{i\omega t} = (P_r, P_\theta, P_z)^T e^{i\omega t}$. At instant t, the force is applied at (R, θ_0–Ωt, Z), where θ_0 is the initial position of the force relative to the wheel. The elastic displacements of a point on the wheel are denoted by $u_r(r,\theta,z,t)$, $u_\theta(r,\theta,z,t)$ and $u_z(r,\theta,z,t)$.

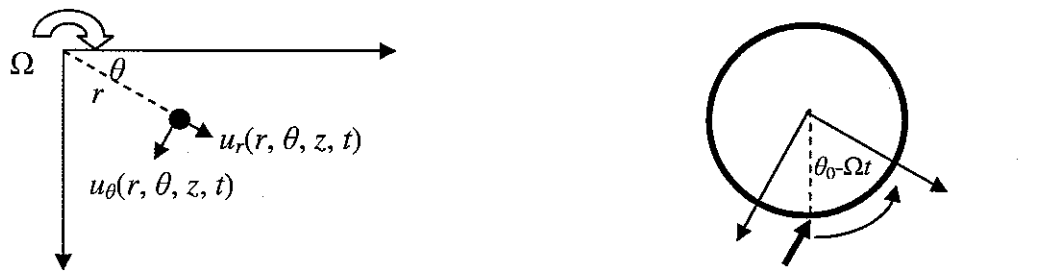

Coordinate system fixed on the wheel

Wheel/rail contact force moving along wheel periphery

Figure 1. Description of the wheel

Thompson [14] considered the dynamics of a railway wheel subject to a rotating load using the finite element (FE) method, with structural effects of rotation, such as centrifugal stiffening and

Coriolis forces, being neglected. The procedures are outlined as follows. First a FE model is established in the cylindrical coordinate system (r, θ, z) for the stationary wheel. From this FE model natural frequencies and mode shapes can be determined. The modes are classified using two subscripts (m, n) instead of one, with n corresponding to the number of nodal diameters in the mode shape. It should be noted that for $n > 0$, these subscripts are not sufficient to define the mode completely: for each (m, n) two independent modes, $\psi_{mn}(r,z)\cos n\theta$ and $\psi_{mn}(r,z)\sin n\theta$, exist, with nodal diameters and anti-nodal diameters transposed, both having the same natural frequency, ω_{mn}, and basic mode shape $\psi_{mn}(r,z)$. The mode shape $\psi_{mn}(r,z)$ may be split into two parts, $\psi^{I}_{mn}(r,z)$ which contains the radial and axial displacement components and $\psi^{II}_{mn}(r,z)$ containing the circumferential displacement component only. Thus the full mode shapes can actually be written as follows:

For even modes (about θ): $\varphi^{e}_{mn}(r,\theta,z) = \psi^{I}_{mn}(r,z)\cos n\theta + \psi^{II}_{mn}(r,z)\sin n\theta$ (3)

For odd modes (about θ): $\varphi^{o}_{mn}(r,\theta,z) = \psi^{I}_{mn}(r,z)\sin n\theta - \psi^{II}_{mn}(r,z)\cos n\theta$ (4)

The corresponding generalised coordinates are denoted by q^{e}_{mn} (q^{o}_{mn}) for the even (odd) modes. For the even modes, the differential equation reads

$$\begin{aligned} &m_{mn}\ddot{q}^{e}_{mn}(t) + c_{mn}\dot{q}^{e}_{mn}(t) + k_{mn}q^{e}_{mn}(t) \\ &= \{\mathbf{P}^{I}\cdot\psi^{I}_{mn}(R,Z)\cos n(\theta_0 - \Omega t) + \mathbf{P}^{II}\cdot\psi^{II}_{mn}(R,Z)\sin n(\theta_0 - \Omega t)\}e^{i\omega t} \end{aligned} \quad (5)$$

where the wheel/rail force vector $\mathbf{P}$ has been split into type I and type II components, $\mathbf{P}^{I}$ and $\mathbf{P}^{II}$, which satisfy

$$\mathbf{P}^{I}\cdot\psi^{II}_{mn}(R,Z) = \mathbf{P}^{II}\cdot\psi^{I}_{mn}(R,Z) = 0 \quad (6)$$

Similarly, for the odd modes,

$$\begin{aligned} &m_{mn}\ddot{q}^{o}_{mn}(t) + c_{mn}\dot{q}^{o}_{mn}(t) + k_{mn}q^{o}_{mn}(t) \\ &= \{\mathbf{P}^{I}\cdot\psi^{I}_{mn}(R,Z)\sin n(\theta_0 - \Omega t) - \mathbf{P}^{II}\cdot\psi^{II}_{mn}(R,Z)\cos n(\theta_0 - \Omega t)\}e^{i\omega t} \end{aligned} \quad (7)$$

The solutions of these equations are given by

$$q^{e}_{mn} = T_{mn}\frac{e^{i(\omega+n\Omega)t}}{2m_{mn}d_{+}(\omega)} + T^{*}_{mn}\frac{e^{i(\omega-n\Omega)t}}{2m_{mn}d_{-}(\omega)} \quad (8)$$

$$q^{o}_{mn} = iT_{mn}\frac{e^{i(\omega+n\Omega)t}}{2m_{mn}d_{+}(\omega)} - iT^{*}_{mn}\frac{e^{i(\omega-n\Omega)t}}{2m_{mn}d_{-}(\omega)} \quad (9)$$

where, the asterisk denotes the complex conjugate, and

$$T_{mn} = \mathbf{P}^{I} \cdot \boldsymbol{\psi}^{I}_{mn}(R,Z)e^{-in\theta_0} + i\mathbf{P}^{II} \cdot \boldsymbol{\psi}^{II}_{mn}(R,Z)e^{-in\theta_0} \tag{10}$$

$$d_{\pm}(\omega) = \omega^2_{mn} - (\omega \pm n\Omega)^2 + 2i\zeta_{mn}(\omega \pm n\Omega)\omega_{mn} \tag{11}$$

in which $\omega^2_{mn} = \frac{k_{mn}}{m_{mn}}$ and $\zeta_{mn} = \frac{c_{mn}}{2\omega_{mn}m_{mn}}$. Now the total displacement of the wheel observed from the wheel itself is given by

$$\mathbf{u}(r,\theta,z,t) = \sum_{m,n}\left\{\psi_{mn}(r,z)T_{mn}\frac{e^{i[(\omega+n\Omega)t+n\theta]}}{2m_{mn}d_{+}(\omega)} + \psi^{*}_{mn}(r,z)T^{*}_{mn}\frac{e^{i[(\omega-n\Omega)t-n\theta]}}{2m_{mn}d_{-}(\omega)}\right\} \tag{12}$$

where $\psi_{mn} = \psi^{I}_{mn} - i\psi^{II}_{mn}$. This consists of two waves for each (m, n) which are rotating in opposite directions, and at different frequencies, $\omega \pm n\Omega$.

The displacement of the wheel observed from a frame of reference moving in the track direction with the wheel centre can be calculated from equation (12) through a coordinate transformation. Particularly the displacement of the wheel at the loading point in this coordinate system is given by letting $\theta = \theta_0 - \Omega t$ in equation (12),

$$\mathbf{w}(R,Z,t) = e^{i\omega t}\sum_{m,n}\left\{\psi_{mn}(R,Z)T_{mn}\frac{e^{in\theta_0}}{2m_{mn}d_{+}(\omega)} + \psi^{*}_{mn}(R,Z)T^{*}_{mn}\frac{e^{-in\theta_0}}{2m_{mn}d_{-}(\omega)}\right\} \tag{13}$$

Equation (13) shows that the displacement of the wheel at the wheel/rail contact point is harmonic irrespective of the rotation of the wheel. Thus direct receptances can be defined for the wheel. Note that, if the wheel centre has no displacement in the vertical direction, then the vertical component from equation (13) is identical to that observed from the ground.

The vertical displacement, *directed upwards*, at the lth contact point on the wheel due to the lth wheel/rail force now is given by

$$w^{W}_{l}(t) = \sum_{j=-\infty}^{\infty} r^{W}_{l}(j\Omega_0)P_{lj}e^{ij\Omega_0 t} \tag{14}$$

where, $r^{W}_{l}(j\Omega_0)$ is the direct receptance of the lth wheel at frequency $j\Omega_0$, which can be evaluated from equation (13). If the wheel is modelled as a rigid body vibrating in the vertical direction, then

$$r^{W}_{l}(j\Omega_0) = \begin{cases} \dfrac{1}{-m_{Wl}(j\Omega_0)^2}, & j \neq 0 \\ \text{to be defined}, & j = 0 \end{cases} \tag{15}$$

where, m_{Wl} denotes the wheel mass.

2.4 THE VERTICAL DISPLACEMENT OF THE RAIL

It is shown in reference [13] that, the vertical displacement of the rail due to a moving harmonic load is a periodic function of time if observation is made within a frame of reference moving with the load. The period is equal to the sleeper-passing time. Formulae have been derived for the calculation of the Fourier coefficients of this periodic function. According to reference [13], the displacement, *directed downwards*, at the *l*th contact point on the rail due to the *k*th wheel/rail force is given by

$$\begin{aligned} w_{lk}^{R}(t) &= \sum_{m=-\infty}^{\infty} P_{km}\left(\sum_{n=-\infty}^{\infty} r_{lkn}^{R}(m\Omega_0)e^{-in\Omega_0 t}\right)e^{im\Omega_0 t} \\ &= \sum_{m=-\infty}^{\infty} P_{km}\left(\sum_{n=-\infty}^{\infty} r_{lk,m-n}^{R}(m\Omega_0)e^{in\Omega_0 t}\right) \\ &= \sum_{n=-\infty}^{\infty}\left(\sum_{m=-\infty}^{\infty} r_{lk,m-n}^{R}(m\Omega_0)P_{km}\right)e^{in\Omega_0 t} \end{aligned} \tag{16}$$

where, $r_{lkn}^{R}(m\Omega_0)$ is the *n*th Fourier coefficient of the time-varying quasi-receptance at the *l*th contact point due to a unit harmonic force of radian frequency $m\Omega_0$ at the *k*th contact point.

2.5 DETERMINATION OF THE WHEEL/RAIL FORCES

It is assumed that the wheels are always in contact with the rail via a linearised Hertz contact spring. The tangential stiffness of the spring at the *l*th contact point is denoted by k_{Hl}, which is calculated at the static component, W_l, of the wheel/rail force. Thus

$$w_l^{W}(t) + \sum_{k=1}^{M} w_{lk}^{R}(t) + \delta_{stl} + (P_l(t) - W_l)/k_{Hl} = \sum_{n=-\infty}^{\infty} Z_n e^{in\beta_0(a_l+ct)} \quad (l = 1, 2\cdots, M) \tag{17}$$

where, δ_{stl} is the static deformation of the contact spring under the static load, W_l; a_l is the initial position (x-coordinate at $t = 0$) of the *l*th wheel; M is the number of the wheels. Note that in equation (17), the rail irregularities are directed upwards. Inserting equations (2), (14) and (16) into equation (17) yields

$$\begin{aligned} &\sum_{n=-\infty}^{\infty} r_l^{W}(n\Omega_0)P_{l,n}e^{in\Omega_0 t} + \sum_{k=1}^{M}\left(\sum_{n=-\infty}^{\infty}\left(\sum_{m=-\infty}^{\infty} r_{lk,m-n}^{R}(m\Omega_0)P_{km}\right)e^{in\Omega_0 t}\right) + \frac{1}{k_{Hl}}\sum_{\substack{n=-\infty \\ n\neq 0}}^{\infty} P_{l,n}e^{in\Omega_0 t} \\ &= -\delta_{stl} + \sum_{n=-\infty}^{\infty} Z_n e^{in\beta_0 a_l} e^{in\Omega_0 t} \end{aligned} \tag{18}$$

This is equivalent to

$$\left(r_l^W(n\Omega_0)+1/k_{Hl}\right)P_{ln}+\sum_{\substack{m=-\infty\\ m\neq 0}}^{\infty}\sum_{k=1}^{M}r_{lk,m-n}^R(m\Omega_0)P_{km}=Z_n e^{in\beta_0 a_l}-\sum_{k=1}^{M}r_{lk,-n}^R(0\Omega_0)W_k \tag{19}$$

where, $n=-\infty,\cdots,\infty, n\neq 0$ and $l=1,2\cdots,M$. For $n=0$, equation (18) gives

$$r_l^W(0\Omega_0)P_{l0}+\sum_{k=1}^{M}\sum_{m=-\infty}^{\infty}r_{lk,m}^R(m\Omega_0)P_{km}=-\delta_{stl},\quad (l=1,2\cdots,M) \tag{20}$$

From equation (19) the unknowns P_{km} ($k=1,2\cdots,M$ and $m=\pm1,\pm2,\cdots$) can be determined, while equation (20) gives the average displacement of the lth wheel

$$w_{Wl}^0=r_l^W(0\Omega_0)P_{l0}=-\sum_{k=1}^{M}\sum_{m=-\infty}^{\infty}r_{lkm}^R(m\Omega_0)P_{km}-\delta_{stl},(l=1,2\cdots,M) \tag{21}$$

Equation (19) contains an infinite number of unknowns. In actual calculation, only a finite number of unknowns, P_{lm}, $l=1,2\cdots,M$ and $m=-N,\cdots,N, m\neq 0$, are determined through the following equation

$$\left(r_l^W(n\Omega_0)+1/k_{Hl}\right)P_{l,n}+\sum_{\substack{m=-N\\ m\neq 0}}^{N}\sum_{k=1}^{M}r_{lk,m-n}^R(m\Omega_0)P_{km}=Z_n e^{in\beta_0 a_l}-\sum_{k=1}^{M}r_{lk,-n}^R(0\Omega_0)W_k \tag{22}$$

where, $l=1,2\cdots,M$ and $n=-N,\cdots,N, n\neq 0$, N is an positive integer. As has been identified in Subsection 2.1, the highest order of harmonics to be included in the roughness is 30; therefore N may be chosen to be 50. Having worked out P_{lm}, $m=-N,\cdots,N$, the spectra of the wheel/rail forces can be plotted and the rail displacement can be determined through equation (16).

Equation (22) may be written in a more compact form

$$[B]_n\{P\}_n+\sum_{\substack{m=-N\\ m\neq 0}}^{N}[C]_{nm}\{P\}_m=\{Z\}_n-[C]_{n0}\{W\},\ (n=-N,\cdots,N,n\neq 0) \tag{23}$$

where the vectors and matrices are defined as follows,

$$\{P\}_m=(P_{1m},P_{2m},\cdots,P_{Mm})^T \tag{24a}$$

$$[B]_n=\begin{bmatrix} r_1^W(n\Omega_0)+1/k_{H1} & \cdots & 0\\ \vdots & \cdots & \vdots\\ 0 & \cdots & r_M^W(n\Omega_0)+1/k_{HM}\end{bmatrix} \tag{24b}$$

$$[C]_{nm}=\begin{bmatrix} r_{11,m-n}^R(m\Omega_0) & \cdots & r_{1M,m-n}^R(m\Omega_0)\\ \vdots & \vdots & \vdots\\ r_{M1,m-n}^R(m\Omega_0) & \cdots & r_{MM,m-n}^R(m\Omega_0)\end{bmatrix} \tag{24c}$$

$$\{Z\}_n = Z_n(e^{in\beta_0 a_1},\cdots,e^{in\beta_0 a_M})^T \tag{24d}$$

$$\{W\} = (W_1,\cdots,W_M)^T \tag{24e}$$

3. RESULTS

In this section, example calculations are performed using the approach derived in the last section. Calculations are carried out first for a single locomotive wheel and then for four such wheels moving over a conventional ballasted track. Each wheel is modelled as a rigid body having mass 1350 kg and a radius of 0.575 m. The static load applied by the wheel is chosen to be 100 kN. The rail is modelled as a Timoshenko beam. A set of typical parameters for the track structure is listed in Table 1. These parameters are for half the structure (*i.e.* a single rail on half sleepers) and correspond to a track with concrete monobloc sleepers and moderately stiff rail pads.

Wheel/rail force spectra, wheel/rail force 'position-histories' (*i.e.* time history plotted against spatial coordinate) and displacement 'position-histories' of the rail at the wheel/rail contact points are presented. These results are produced for different travelling speeds and different excitation frequencies. The excitation frequencies are defined as the wheel travelling speeds divided by the wavelengths of the vertical railhead profile. The vertical railhead profile is set to be of a single wavelength and the amplitude is chosen to be 10 μm (17 dB re 1 μm), *i.e.* $Z(x) = 1\times10^{-5}\cos\frac{2\pi}{\lambda}x = 1\times10^{-5}\cos\frac{2\pi f}{c}x$ (m), where $x = 0$ is selected to be at a sleeper, f denotes the excitation frequency, c denotes the wheel speed and λ the wavelength (see Table 2). The sleeper-passing frequencies at 20 m/s, 40 m/s and 80 m/s are 34 Hz, 67 Hz and 133 Hz for a sleeper-spacing of 0.6 m. Responses to the parametric excitation are produced by assuming a smooth railhead. The wheel/rail force spectra are discrete with values only at the sleeper-passing frequency and its multiples; however they are plotted as continuous. The displacement of the rail is plotted as positive values if it moves downwards. No wheel displacement is shown here.

TABLE 1 *Parameters for the vertical dynamics of a track*

Density of the rail	$\rho = 7850$ kg/m^3
Young's modulus of the rail	$E = 2.1\times10^{11}$ N/m^2
Shear modulus of the rail	$G = 0.81\times10^{11}$ N/m^2
Loss factor of the rail	$\eta_R = 0.01$
Cross-sectional area of the rail	$A = 7.69\times10^{-3}$ m^2
Second moment of area of the rail cross-section	$I = 30.55\times10^{-6}$ m^4
Shear coefficient of the rail cross-section	$\kappa = 0.4$
Vertical rail pad stiffness	$k_{Pv} = 3.5\times10^8$ N/m
Rail pad loss factor	$\eta_P = 0.25$
Mass of sleeper	$m_S = 162$ kg
Sleeper spacing	$l = 0.6$ m
Vertical ballast stiffness	$k_{Bv} = 50\times10^6$ N/m
Loss factor of ballast	$\eta_B = 1.0$

TABLE 2 *Wavelengths of the roughness in metres at different excitation frequencies and wheel speeds*

Excitation frequencies	Wheel speed 20 m/s	Wheel speed 40 m/s	Wheel speed 80 m/s
533 Hz	0.038	0.076	0.152
1000 Hz	0.02	0.04	0.08
2000 Hz	—	0.02	0.04

3.1 RECEPTANCE OF THE RAIL

In order to interpret the results for the wheel/rail interactions, the vertical receptance (displacement divided by a stationary harmonic load) of the rail is first shown in Figure 2. Results are given at two loading points, above a sleeper and at the mid-span [13]. Also shown are the receptances of the wheel and the contact spring of stiffness 1.4×10^9 N/m. There are three peaks and three dips in the rail receptance that can be identified in this figure. The peak at about 75 Hz is due to the resonance of the track mass (the rail and sleepers vibrate in phase) on the stiffness of the ballast. The dip at 200 to 300 Hz corresponds to the resonance of the sleepers on their supports (rail and ballast), acting as vibration absorbers to the rail. The peak at about 500 Hz corresponds to the resonance of the rail and sleeper out-of-phase, and to a large extent is determined by the railpad stiffness. The peak/dip at about 1000 Hz indicates the so-called pinned-pinned vibration of the rail on its supports. At this frequency, the wavelength of the rail equals twice the sleeper spacing and the maximum amplitude occurs at the mid-span while the minimum amplitude occurs at the sleepers. A second pinned-pinned frequency is also observed at about 2800 Hz in which the wavelength is equal to the sleeper spacing and the mid-span, in addition to the sleepers, also behaves as a node. Therefore a dip appears for the loading point either at the mid-span or above a sleeper. A wheel-on-track resonance of the combined system will occur when the magnitudes of the wheel and track receptances are equal, at approximately 50 Hz.

If the harmonic load is moving, then the ratio of the displacement of the loading point to the load is not a constant but is a periodic function of time with a period equal to the sleeper-passing time. Therefore the conventional definition of receptance cannot be applied for a moving load. However one may plot the ratio at a particular instant (e.g. $t = 0$), or position, against the frequency of the load, as shown in Figure 3. The main difference between such a plot and that in Figure 2 is that the peak at the pinned-pinned frequency is split into two lower peaks by the load speed. The frequency separation of these two peaks increases with the load speed. The depth of the dip at the first pinned-pinned frequency and that at the second are also reduced by the load speed. However, the split of the dips is observable only at the second pinned-pinned frequency.

For frequencies much lower or greater than the pinned-pinned frequency (referred to the first one if not specified), the response of the rail at the loading point does not significantly depend on the position of the loading, indicating that the rail behaves as if it were continuously supported.

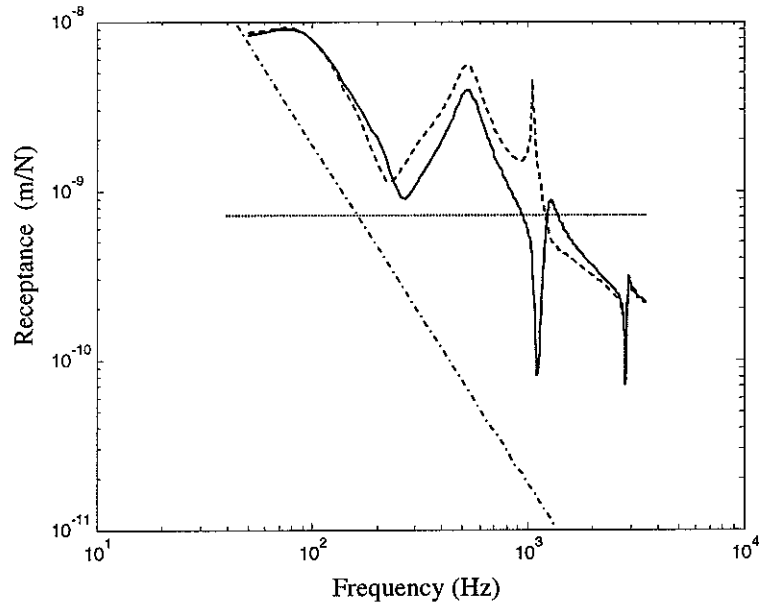

Figure 2. Vertical receptance of the rail at the loading point. ——, above sleeper; – – –, at the mid-span. – · –, for the wheel; ……, for the contact spring.

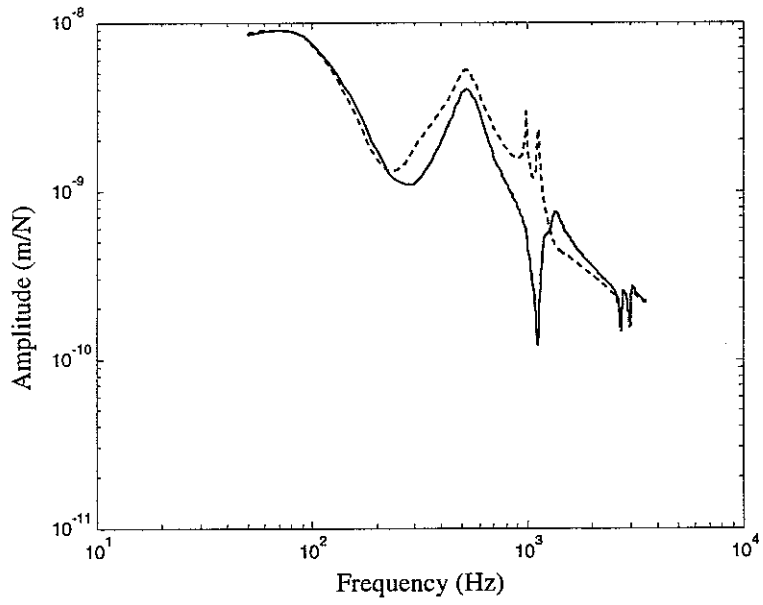

Figure 3. Response of the rail at the loading point for load speed = 80 m/s. ——, above sleeper; – – –, at the mid-span.

3.2 A SINGLE WHEEL MOVING ALONG THE RAIL

3.2.1 RAIL WITH A SMOOTH RAILHEAD

For the rail with a smooth railhead, the results are shown in Figures 4 to 6. It is seen from Figure 4 that the wheel/rail force spectrum shows a second peak near the pinned-pinned frequency (about 1000 Hz), in addition to the first peak at 0 Hz which corresponds to the static load. The magnitude of this peak, however, is much less than the component at the sleeper-passing frequency (67 Hz at 40 m/s), even at very high speeds. A dip is observed at about 500 Hz which is caused by the low stiffness (high receptance, see Figure 3) of the rail.

The dynamic wheel/rail force increases as the wheel speed increases (Figures 4 and 5). Table 3 shows the ratios of the first three components of the dynamic wheel/rail force to the static load. At speeds below 40 m/s, the component at the sleeper-passing frequency is dominant. However, for higher wheel speeds, the second component at twice the sleeper-passing frequency can be as strong as the first one. This is because the frequency of the second component is within the frequency range (200 to 300 Hz) within which the rail receptance has a dip.

TABLE 3 *Ratios of the first three components of the wheel/rail force to the static load*

Wheel speed	First component	Second component	Third component
0.01 m/s	0.0%	0.0%	0.0%
20 m/s	1.4%	0.4%	0.0%
40 m/s	2.0%	0.6%	0.4%
60 m/s	2.0%	2.1%	0.4%
80 m/s	3.4%	2.3%	0.4%

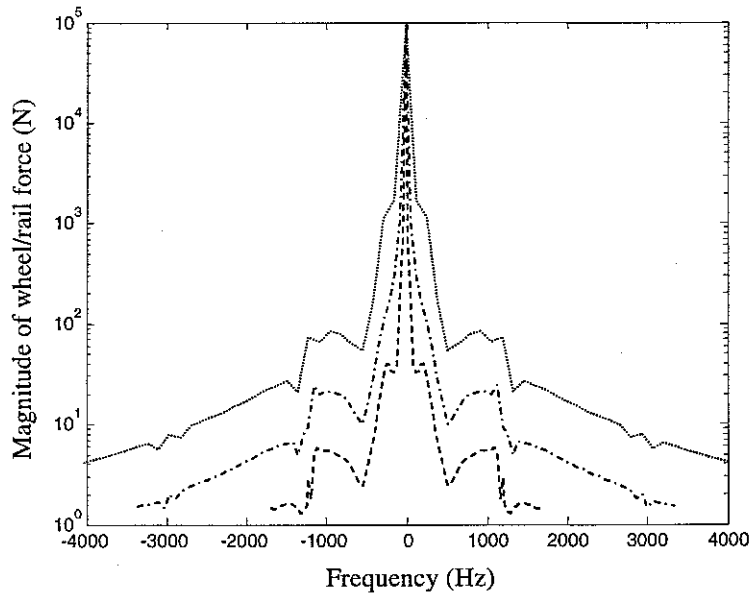

Figure 4. Wheel/rail force spectrum for the wheel moving at 20 m/s (– – –), 40 m/s (– · –) and 80 m/s (……) over the rail with a smooth railhead.

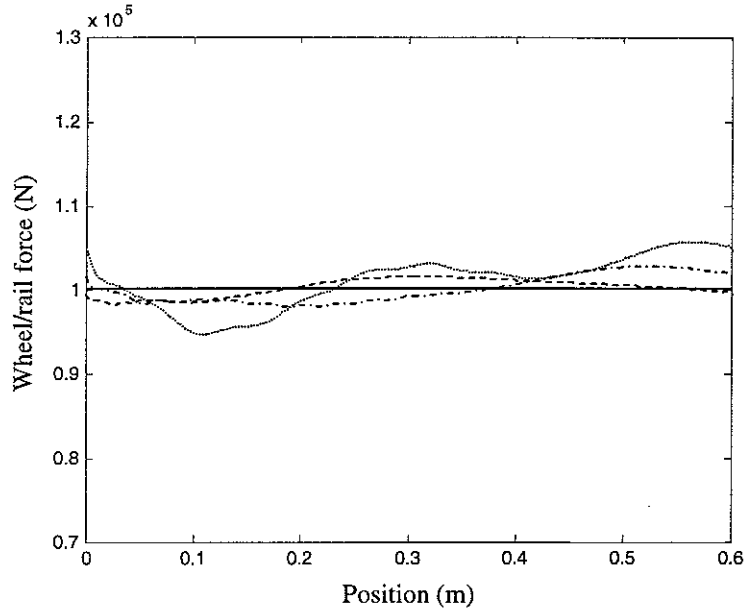

Figure 5. Wheel/rail force position-history for the wheel moving at 0.01 m/s (——), 20 m/s (– – –), 40 m/s (– · –) and 80 m/s (……) over the rail with a smooth railhead.

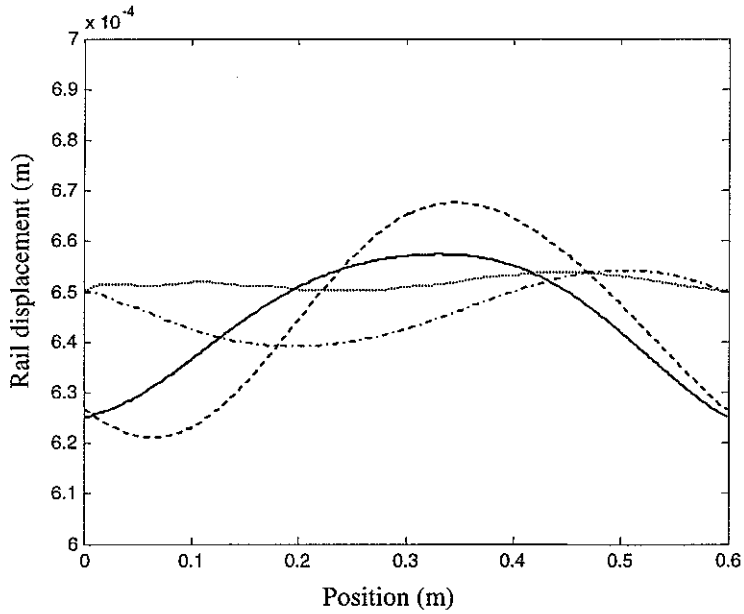

Figure 6. Rail displacement position-history for the wheel moving at 0.01 m/s (——), 20 m/s (– – –), 40 m/s (– · –) and 80 m/s (……) over the rail with a smooth railhead.

At low wheel speeds (less than 20 m/s), the rail deformation (Figure 6) shows a static feature. There exists a resonance phenomena speed which is approximately 30 m/s. When the wheel moves at this speed, the wheel-on-track resonance, which is about 50 Hz as identified in Sub-section 3.1, is excited by the sleeper-passing of the wheel. When the wheel moves at speeds higher than this speed, the static deformation feature disappears and the variation of the displacement of the rail at the loading becomes smaller as the wheel speed increases, and the track behaves as if it were continuously supported.

3.2.2 RAIL WITH A SPATIALLY HARMONIC RAILHEAD

Figures 7 to 9 show the spectra of the wheel/rail force for the wheel moving over the rail with sinusoidal roughness at frequencies 533 Hz, 1000 Hz and 2000 Hz. From these figures, it can be seen that, in addition to the peaks at 0 Hz and the pinned-pinned frequency, the wheel/rail force spectra have a peak at the excitation frequency. Although the magnitudes of other harmonic components (they are mainly caused by the parametric excitation) increase with the wheel speed, the magnitude of the component at the excitation frequency is almost independent of the wheel speed at these excitation frequencies. The magnitude of the harmonic component at the excitation frequency is shown in Figure 10 for a range of excitation frequencies.

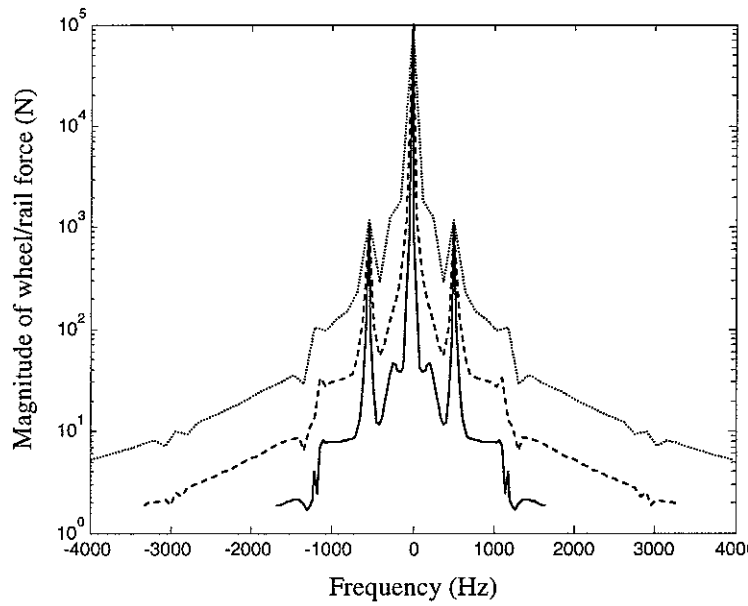

Figure 7. Wheel/rail force spectrum for the wheel moving at 20 m/s (——), 40 m/s (– – –) and 80 m/s (.....) over the rail with a sinusoidal railhead of amplitude 10 μm at a wavelength corresponding to 533 Hz.

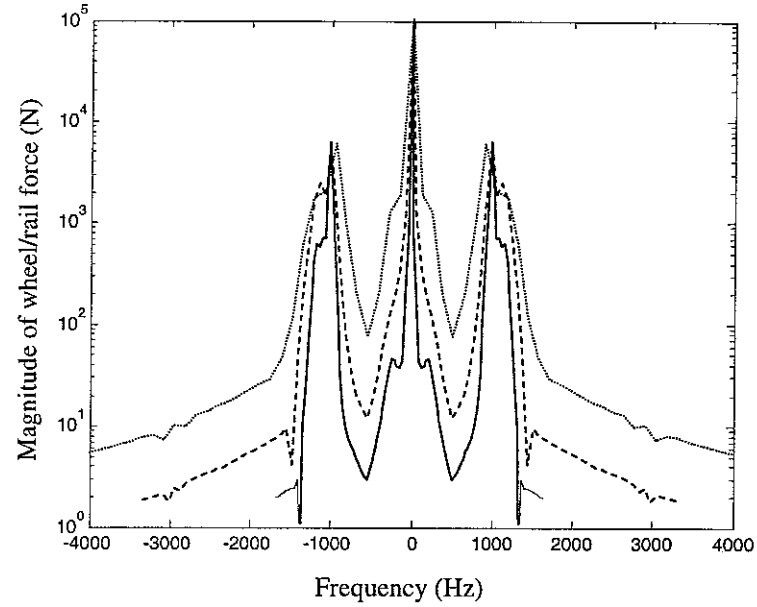

Figure 8. Wheel/rail force spectrum for the wheel moving at 20 m/s (——), 40 m/s (– – –) and 80 m/s (.....) over the rail with a sinusoidal railhead of amplitude 10 μm at a wavelength corresponding to 1000 Hz.

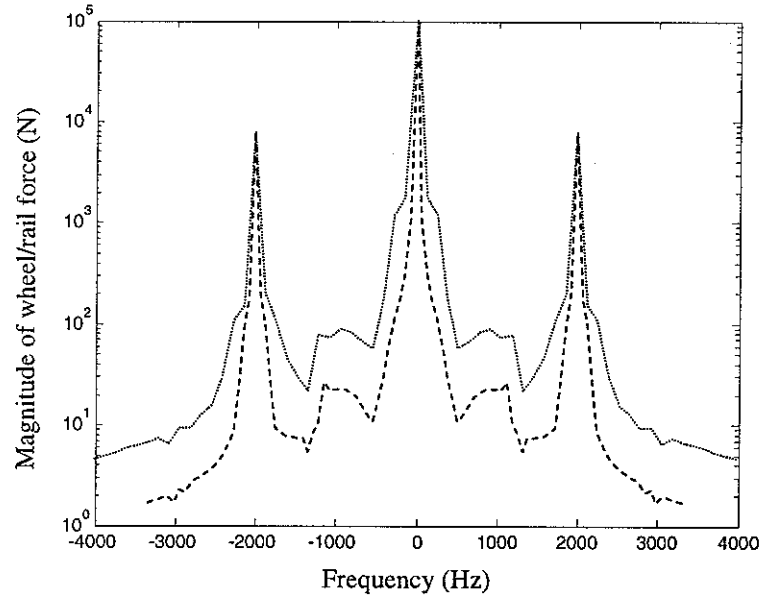

Figure 9. Wheel/rail force spectrum for the wheel moving at 40 m/s (– – –) and 80 m/s (.....) over the rail with a sinusoidal railhead of amplitude 10 μm at a wavelength corresponding to 2000 Hz.

From Figure 10 it can be seen that, at frequencies below the pinned-pinned frequency, there is a correspondence between the peaks (dips) in this figure and the dips (peaks) in the receptance of the rail shown in Figure 2. In other words, high stiffness of the rail leads to a high wheel/rail force. The effect of the wheel speed is negligible for this frequency range and the small variation at the first dip and peak for different wheel speeds is an effect of the limited frequency resolution. Around the first pinned-pinned frequency (from 1000 Hz to 1350 Hz, which corresponds to the intersections of the receptance of the contact spring with that of the track in Figure 2), the magnitude of the

harmonic component at the excitation frequency presents a 'peak-dip-peak' pattern and this zigzag pattern gradually disappears as the wheel speed increases. This feature distinguishes the 'moving wheel model' from the 'moving roughness model': in the latter, the dynamic wheel/rail force presents a peak at the pinned-pinned frequency if the wheel is above a sleeper; on the other hand, if the wheel is at the mid-span, a dip occurs in the dynamic wheel/rail force at the pinned-pinned frequency. Figure 10 also shows that for frequencies higher than the first pinned-pinned frequency, the magnitude of the harmonic component at the excitation frequency is almost a constant. This is because for these frequencies, the receptance of the contact spring is dominant over those of the track and the wheel. However, at the second pinned-pinned frequency, a small dip (instead of a peak) appears and it becomes less obvious as the wheel speed increases.

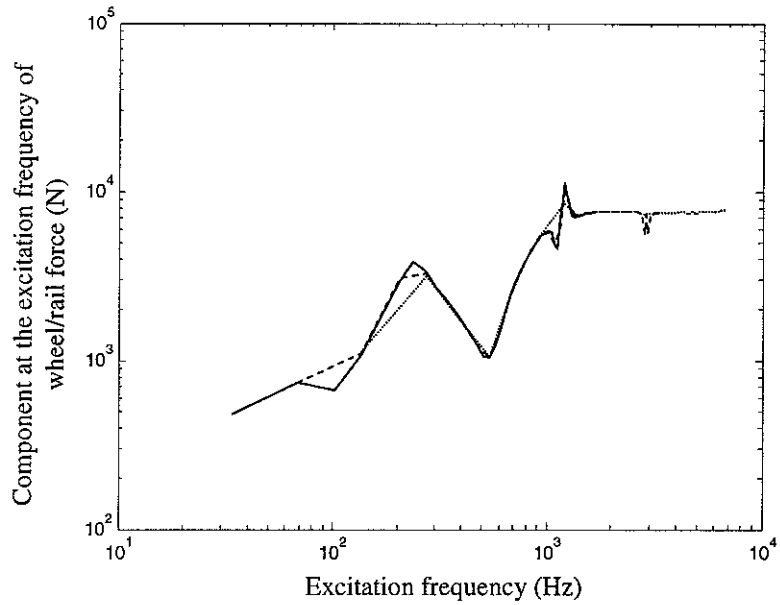

Figure 10. The component of the wheel/rail force at the excitation frequency for the wheel moving at 20 m/s (——), 40 m/s (– – –) and 80 m/s (……) over the rail with a sinusoidal railhead of amplitude 10 μm.

The dynamic wheel/rail force position-history induced by the irregular rail profile only (the component due to the wheel moving over the rail with a smooth railhead is subtracted from the total wheel/rail force) is shown in Figures 11 to 13. In each figure the history is plotted for a single sleeper bay and the excitation frequency is fixed, so the wavelength increases as the wheel speed increases. At frequencies much lower (Figure 11) or higher (Figure 13) than the pinned-pinned frequency, the dynamic wheel/rail force due to the rail irregularity is basically harmonic, following the pattern of the irregularity. This is confirmed by the wheel/rail force spectra shown in Figures 7 and 9 in which a narrow and sharp peak occurs at the excitation frequency. The wheel speed does not have a significant effect at these frequencies. However near the pinned-pinned frequency (Figure 12), the wheel/rail force history exhibits a complex pattern. As shown in Figure 8, harmonic components of similar order exist around the excitation frequency and these harmonic components

modulate each other, giving a complex resultant wheel/rail force history. A strong effect of the wheel speed is clearly revealed in Figure 12: the maximum wheel/rail force is shifted by the wheel speed from the sleeper towards the mid-span.

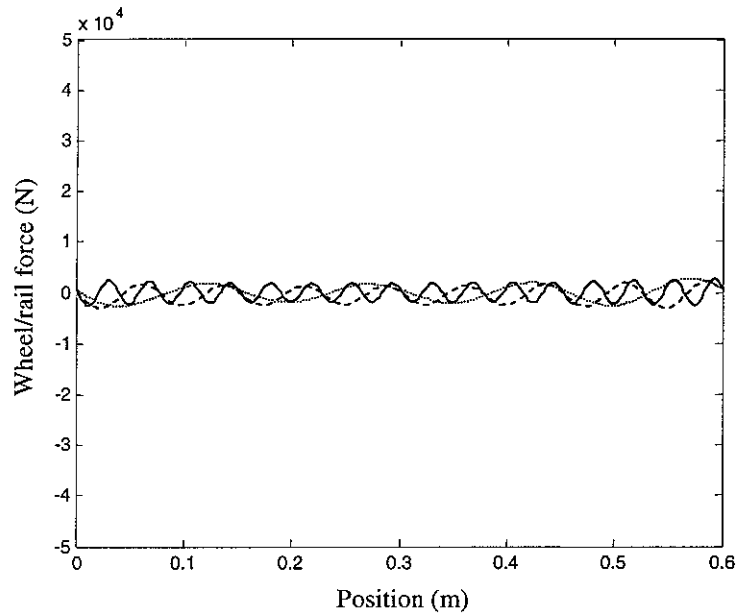

Figure 11. Wheel/rail force position-history for the wheel moving at 20 m/s (——), 40 m/s (– – –) and 80 m/s (……) over the rail with a sinusoidal railhead of amplitude 10 μm at a wavelength corresponding to 533 Hz.

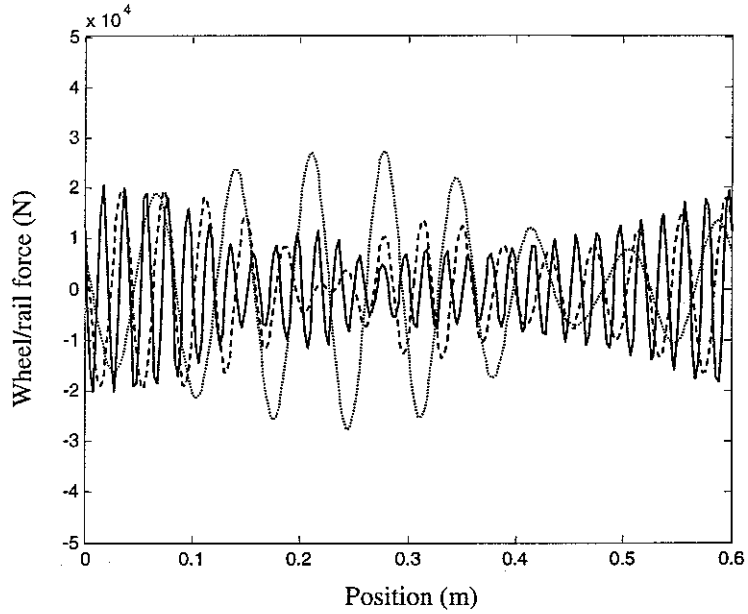

Figure 12. Wheel/rail force position-history for a wheel moving at 20 m/s (——), 40 m/s (– – –) and 80 m/s (……) over the rail with a sinusoidal railhead of amplitude 10 μm at a wavelength corresponding to 1000 Hz.

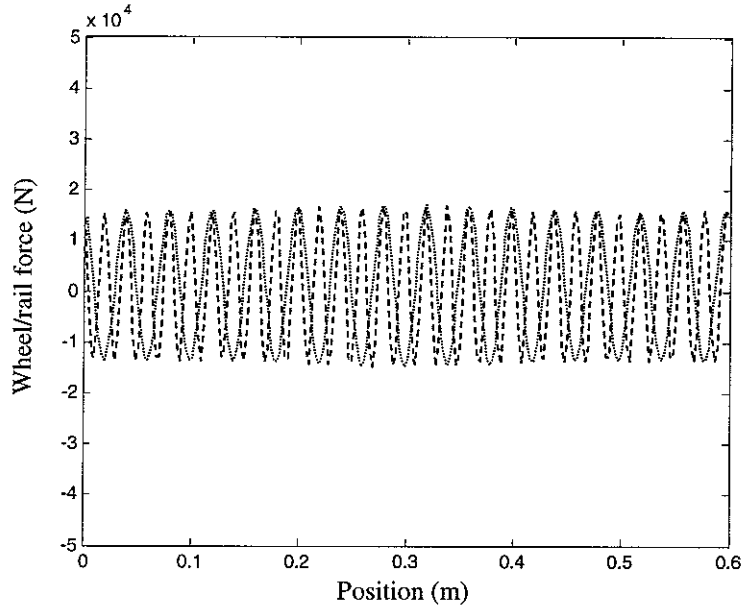

Figure 13. Wheel/rail force position-history for the wheel moving at 40 m/s (– – –) and 80 m/s (.....) over the rail with a sinusoidal railhead of amplitude 10 μm at a wavelength corresponding to 2000 Hz.

The displacement position-history of the rail at the wheel/rail contact point is shown in Figures 14 to 16 for the three excitation frequencies, *i.e.* 553 Hz, 1000 Hz and 2000 Hz respectively. Only the displacement generated by the irregular rail profile is shown in these figures, excluding that due to the parametric excitation (Figure 6). The rail displacement contains the same feature as the wheel/rail force. At frequencies much lower (Figure 14) or higher (Figure 16) than the pinned-pinned frequency, the rail displacement is almost harmonic, and the wheel speed almost has no effect on the amplitude of the displacement. At 533 Hz, since the both the receptances of the wheel and contact spring are much smaller than that of the rail (Figure 2), the roughness is absorbed totally by the rail, as a result, the rail experiences dynamic displacement of the same amplitude (10 μm) as the roughness. At 2000 Hz, half the roughness is absorbed by the contact spring. These observations are not true for frequencies near the pinned-pinned frequency, but instead, the wheel speed does have a strong effect on the rail displacement which is far different from a harmonic response.

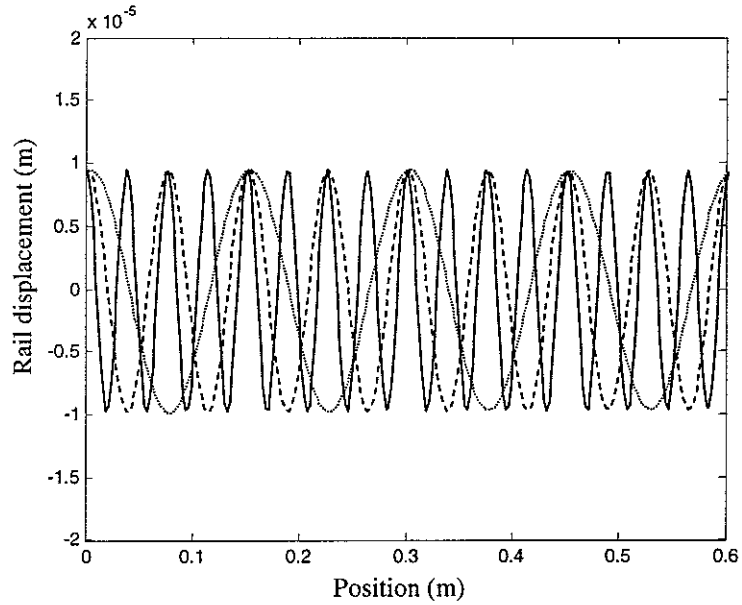

Figure 14. Rail displacement position-history for the wheel moving at 20 m/s (——), 40 m/s (– – –) and 80 m/s (.....) over the rail with a sinusoidal railhead of amplitude 10 μm at a wavelength corresponding to 533 Hz.

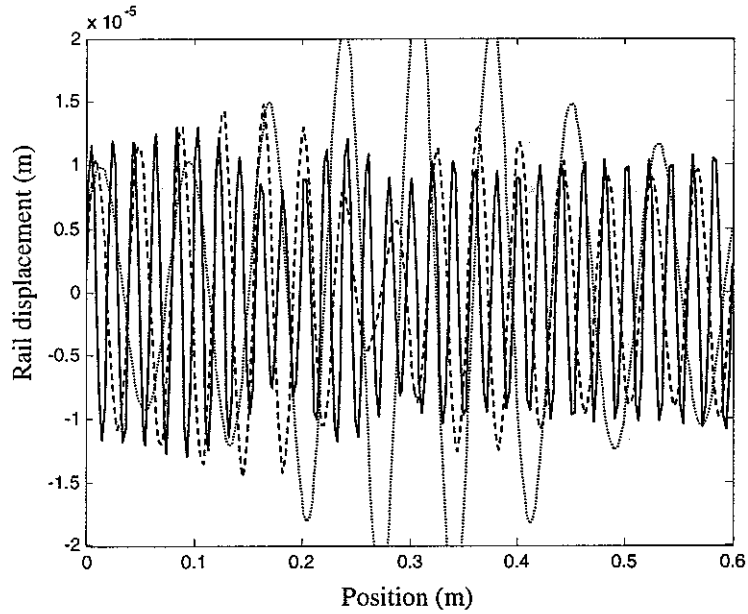

Figure 15. Rail displacement position-history for the wheel moving at 20 m/s (——), 40 m/s (– – –) and 80 m/s (.....) over the rail with a sinusoidal railhead of amplitude 10 μm at a wavelength corresponding to 1000 Hz.

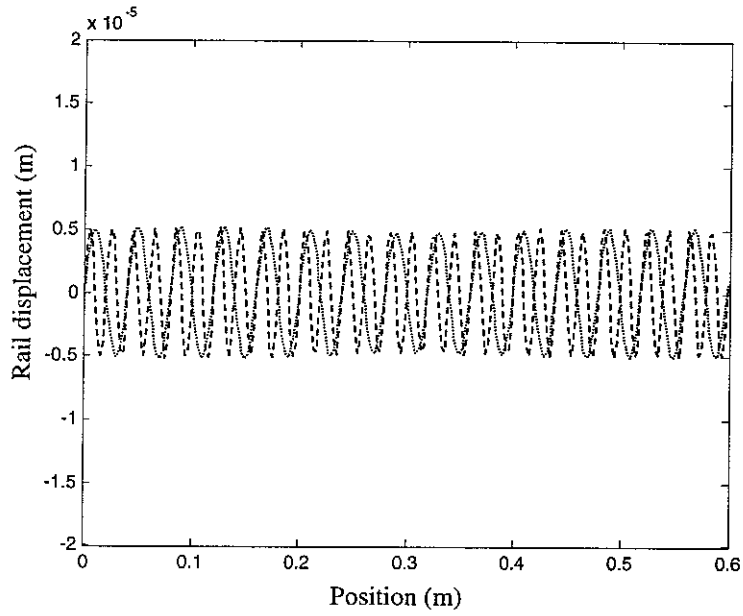

Figure 16. Rail displacement position-history for the wheel moving at 40 m/s (– – –) and 80 m/s (.....) over the rail with a sinusoidal railhead of amplitude 10 μm at a wavelength corresponding to 2000 Hz.

3.3 FOUR WHEELS MOVING ALONG THE RAIL

Now discussion is turned to the case in which there are four wheels from two bogies at the rail. The bogie wheelbase is 3.3 m long and the distance between the bogie centres is 10 m, *i.e.* $a_1 = 0$ m, $a_2 = -3.3$ m, $a_3 = -10$ m and $a_4 = -13.3$ m.

3.3.1 RAIL WITH A SMOOTH RAILHEAD

For the rail with a smooth railhead, the wheel/rail forces and the displacements of the rail at the wheel/rail contact points are shown in Figure 17 to Figure 20, for two wheel speeds, 20 m/s and 40 m/s. There results are produced for the wheels passing the same sleeper bay.

Figures 17 and 18 show the wheel/rail forces of the four wheels. Since the bogie wheelbase is relatively short, the wheel/rail forces within a bogie are indistinguishable. However, a phase shift is clearly present between the two bogies due to the different propagation properties ahead and behind a moving load (see below).

Compared with Figure 5 for a single wheel, the wheel/rail forces of the first bogie are almost identical to that of the single wheel. This indicates that the effects of the last two wheels on the first two wheel/rail forces are negligible.

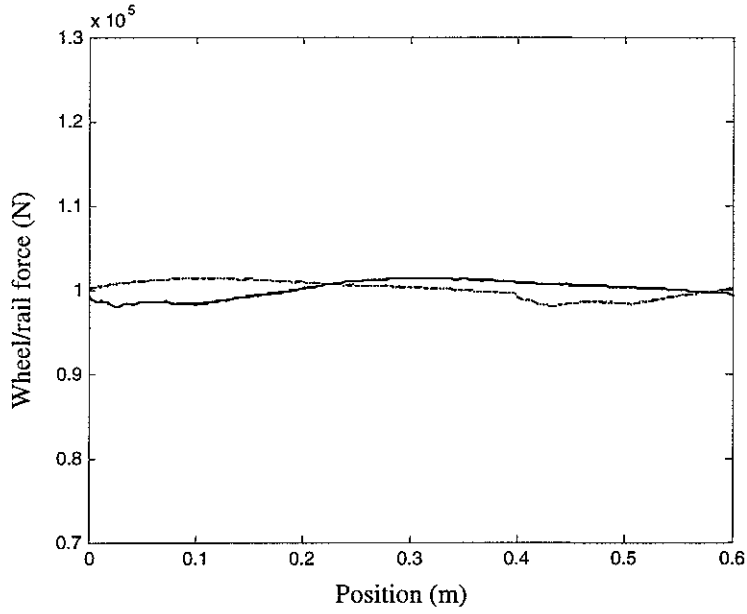

Figure 17. Wheel/rail force position-history for the wheels moving at 20 m/s over the rail with a smooth railhead. ——, at the first wheel; – – –, at the second; – · –, at the third; ....., at the fourth.

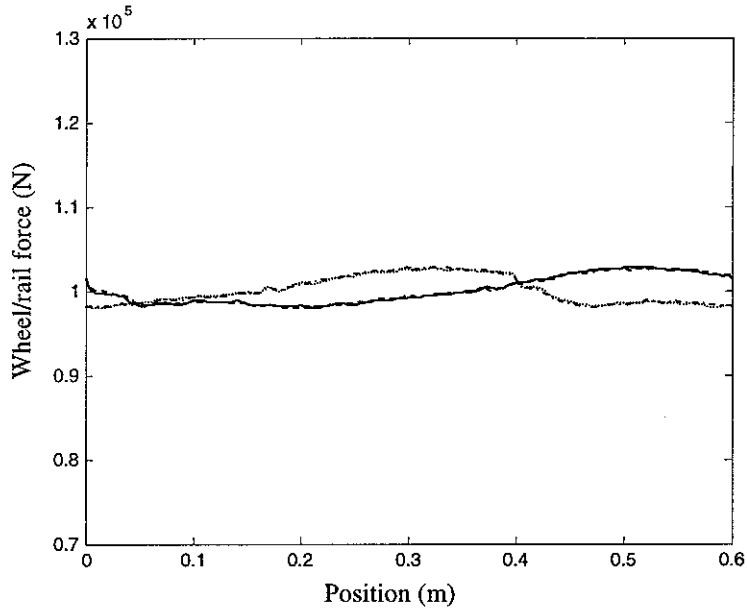

Figure 18. Wheel/rail force position-history for the wheels moving at 40 m/s over the rail with a smooth railhead. ——, at the first wheel; – – –, at the second; – · –, at the third; ....., at the fourth.

Figures 19 and 20 show the rail displacements at the wheel/rail contact points within the same sleeper bay. Subject to a single stationary static load, the deformation of the rail ahead and behind the load is symmetric. This symmetry disappears if the load is moving and the displacement of the rail ahead of the load becomes negative beyond a certain distance (upwards), while that at and behind the load remains positive and becomes greater. Because of this effect of the wheel speed, the rail displacement at the first wheel/rail contact point is the lowest while at the last wheel/rail contact point the rail displacement is the greatest.

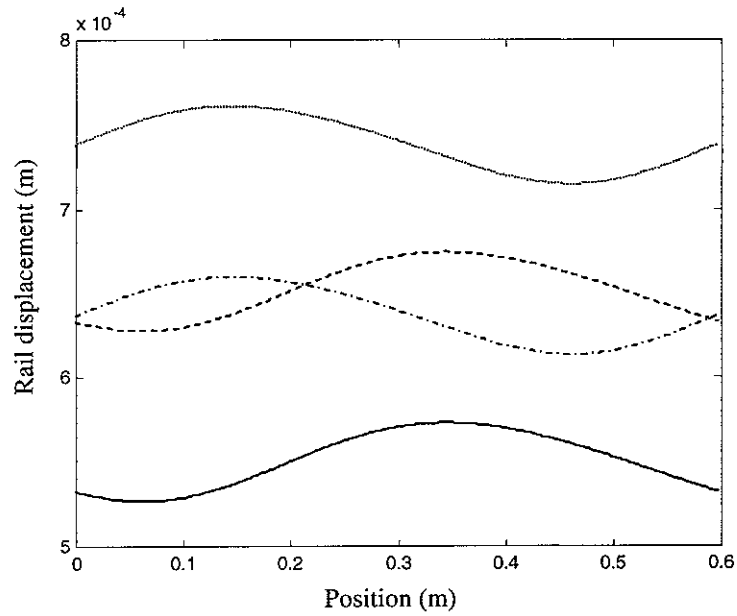

Figure 19. Rail displacement position-history for the wheels moving at 20 m/s over the rail with a smooth railhead. ——, at the first wheel; – – –, at the second; – · –, at the third; ....., at the fourth.

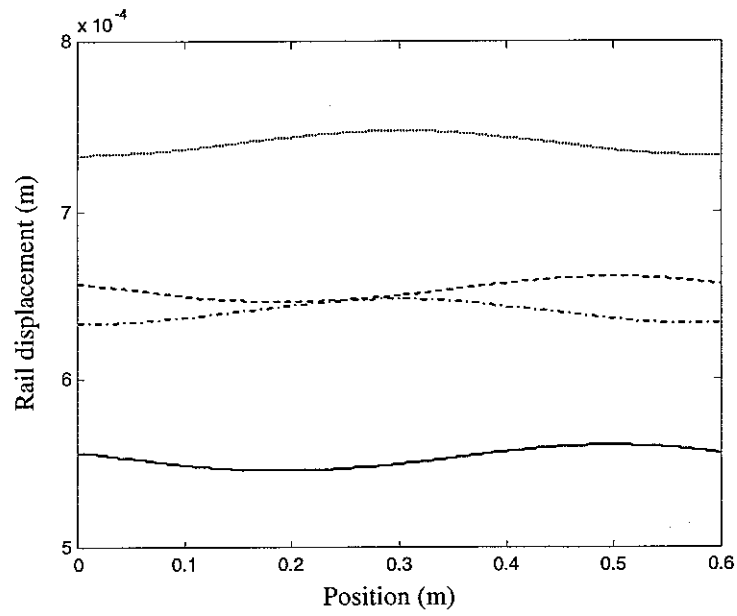

Figure 20. Rail displacement position-history for the wheels moving at 40 m/s over the rail with a smooth railhead. ——, at the first wheel; – – –, at the second; – · –, at the third; ....., at the fourth.

3.3.2 RAIL WITH A SPATIALLY HARMONIC RAILHEAD

For the wheels moving at 20 m/s and 40 m/s over the rail with a spatially harmonic railhead of a single wavelength, the results are shown in Figures 21 to 27.

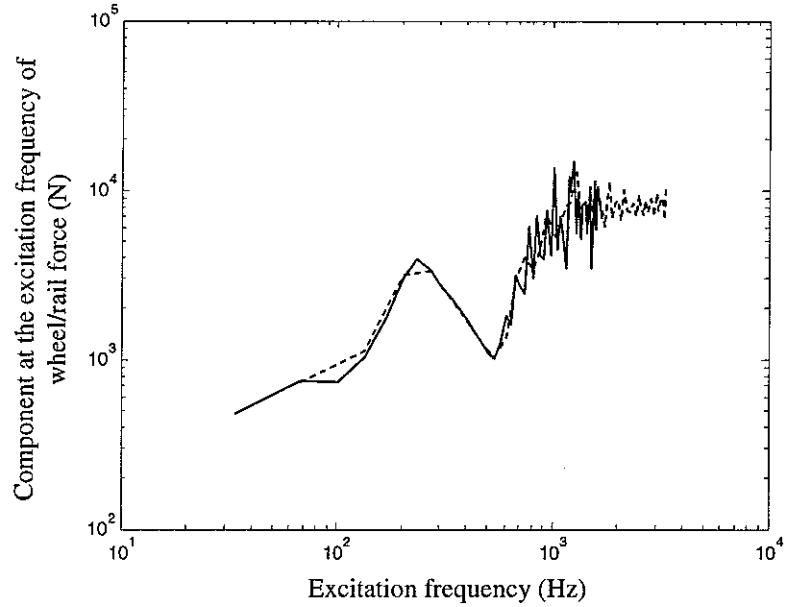

Figure 21. The component at the excitation frequency of the first wheel/rail force for the wheel moving at 20 m/s (——) and 40 m/s (– – –) over the rail with a sinusoidal railhead of amplitude 10 μm.

The harmonic component at the excitation frequency of the first wheel/rail force is shown in Figure 21. At frequencies below 600 Hz, this component presents almost no difference from that in the single wheel case shown in Figure 10. In other words, for those frequencies, interactions between the wheels are negligible. However, at higher frequencies, many strong peaks which are not found in Figure 10 appear here showing the interactions between the multiple wheels. The wheel speed mitigates the effects from other wheels on the first one due to the non-symmetric wave propagations ahead of and behind a moving wheel. Around the pinned-pinned frequency, the wheel speed, as in the single wheel case, has a strong effect on the wheel/rail forces (Figures 22 and 23), and different wheel/rail contact points present different wheel/rail force patterns due to the interactions between them.

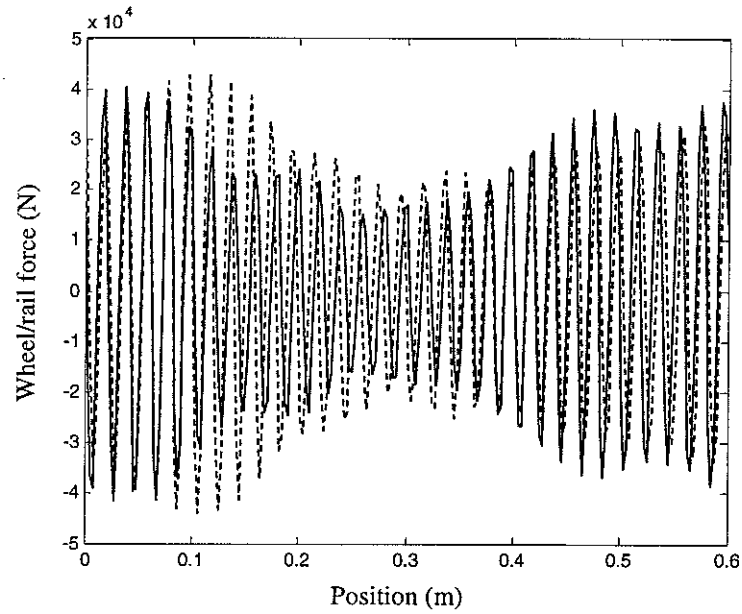

Figure 22. Wheel/rail force position-history for the wheels moving at 20 m/s over the rail with a sinusoidal railhead of amplitude 10 μm at a wavelength corresponding to 1000 Hz. ——, at the first wheel; – – –, at the second wheel.

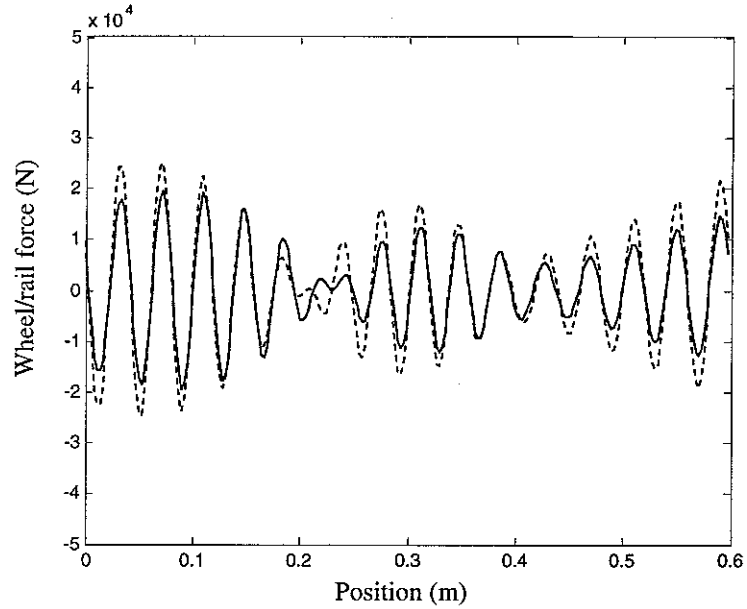

Figure 23. Wheel/rail force position-history for the wheels moving at 40 m/s over the rail with a sinusoidal railhead of amplitude 10 μm at a wavelength corresponding to 1000 Hz. ——, at the first wheel; – – –, at the third wheel.

The displacement position-histories of the rail at the wheel/rail contact points are shown in Figures 24 to 26 for excitation frequency being 1000 Hz and 2000 Hz respectively. At 1000 Hz, both the pinned-pinned effect and the interactions between the wheels contribute to form the complex patterns depending on the wheel speed as well as the wheel position, and the displacements are much stronger than that in the single wheel case (Figure 15). At 2000 Hz, the rail displacements at both the first wheel and the third one are basically harmonic, with the

displacement at the third wheel is much greater that that at the first wheel due to the wave propagations.

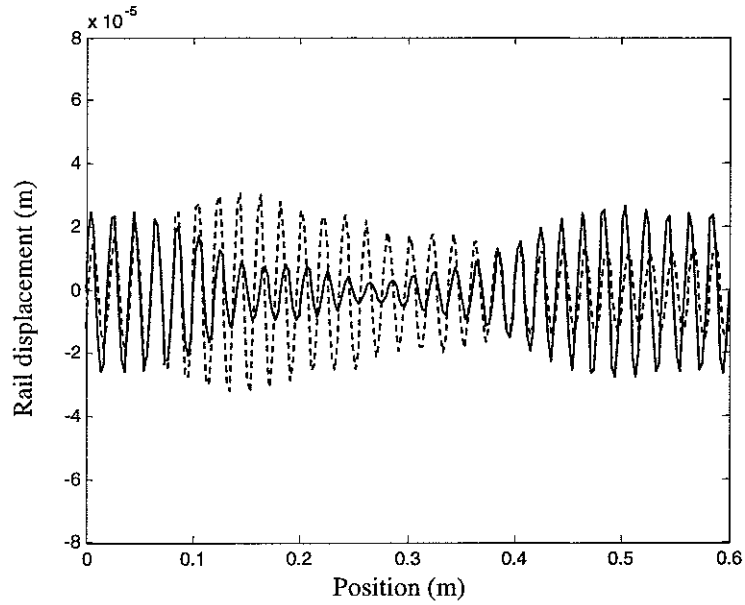

Figure 24. Rail displacement position-history for the wheels moving at 20 m/s over the rail with a sinusoidal railhead of amplitude 10 μm at a wavelength corresponding to 1000 Hz. ——, at the first wheel; – – –, at the second wheel.

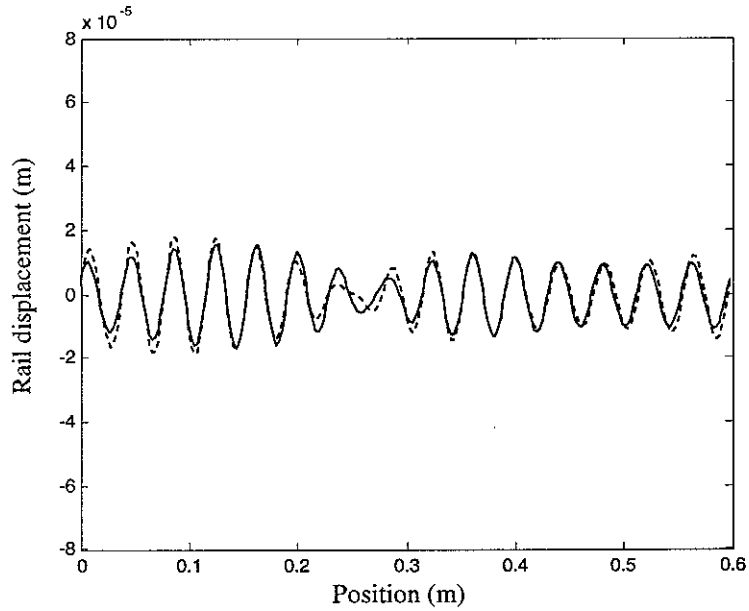

Figure 25. Rail displacement position-history for the wheels moving at 40 m/s over the rail with a sinusoidal railhead of amplitude 10 μm at a wavelength corresponding to 1000 Hz. ——, at the first wheel; – – –, at the third wheel.

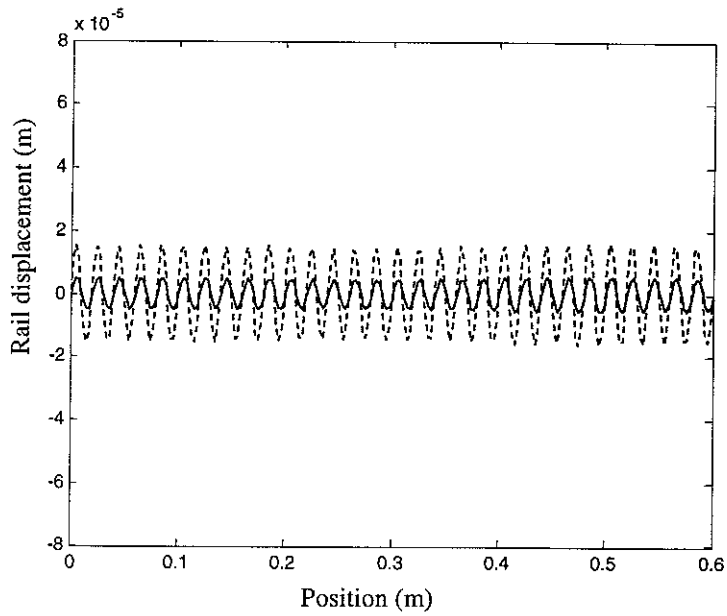

Figure 26. Rail displacement position-history for the wheels moving at 40 m/s over the rail with a sinusoidal railhead of amplitude 10 μm at a wavelength corresponding to 2000 Hz. ——, at the first wheel; – – –, at the third wheel.

3.4 ROUGHNESS EQUIVALENT TO THE PARAMETRIC EXCITATION

Equation (22) shows that there are two excitation mechanisms, the roughness defined by $Z_n e^{in\beta_0 a_l}$ and the parametric excitation given by $\left(-\sum_{k=1}^{M} r^R_{lk,-n}(0\Omega_0)W_k\right)$, where, $l = 1, 2\cdots, M$ and $n = -N, \cdots, N, n \neq 0$. The nth component of an equivalent roughness at the lth wheel may be defined as

$$Z^e_{l,n} = -e^{-in\beta_0 a_l}\sum_{k=1}^{M} r^R_{lk,-n}(0\Omega_0)W_k \ , (n = -N, \cdots, N, n \neq 0) \tag{25a}$$

$$Z^e_{l,0} = 0 \tag{25b}$$

and the roughness is given by summing these components

$$z^e_l(x) = \sum_{n=-N}^{N} Z^e_{l,n} e^{in\beta_0 x} = -\sum_{\substack{n=-N \\ n\neq 0}}^{N}\left(\sum_{k-1}^{M} r^R_{lk,-n}(0\Omega_0)W_k\right)e^{in\beta_0(x-a_l)} \tag{26}$$

The equivalent roughness may be input into a 'moving roughness model' so that it can account for the parametric excitation. Equation (25) shows that for different wheels the equivalent roughness is different. The equivalent roughness depends on the wheel speed, the static loads and the track dynamics, but is independent of the wheel dynamics. It is the position-varying displacement of the rail at a wheel under the action of the moving static load that causes parametric excitation. The greater the static (axle load), the stronger is the parametric excitation. This is why

parametric excitation is of more concern for heavy freight trains. If the rail is continuously supported, then no parametric excitation is expected.

The roughness levels equivalent to the parametric excitation are calculated according to equation (25), and shown in Figure 27 for a single wheel moving at 20 m/s, 40 m/s and 80 m/s along the track. The levels for the first two speeds are indistinguishable and for the highest speed the roughness level is increased by about 3 dB only at wavelength 0.3 m, half the sleeper spacing. At wavelengths of 0.3 m and 0.6 m, the roughness levels are greater than 0 dB and even can be as high as more than 10 dB, comparable to some actual roughness present on main railway lines. Equation (25) shows that doubling the static load, the equivalent roughness levels will be increased by 6 dB.

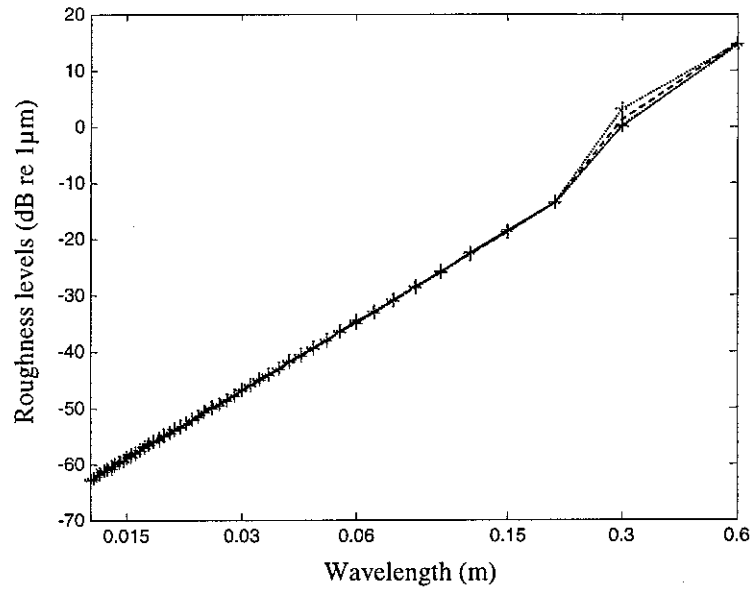

Figure 27. Roughness levels equivalent to the parametric excitation. ——, at wheel speed 20 m/s; – · –, 40 m/s; ……, 80 m/s; – – –, for the soft pads at 40 m/s.

To identify the effect of the railpad stiffness, the equivalent roughness levels are produced for the railpad stiffness being 70 MN/m and other parameters being kept unchanged. The result is also shown in Figure 32 in dashed line. It can be seen that the equivalent roughness levels are slightly increased at wavelength 0.3 m.

4. CONCLUSION

Using the wavenumber-based method of calculating the response of a periodically supported rail to a moving harmonic load, the interactions between a single, or multiple moving wheels and a railway track are formulated and investigated in this report. Instead of using time-domain approaches which are normally employed to account for the travelling of the wheels, this approach

works in the frequency-domain and therefore it can account for high frequency vibration and the results from this model are easier to interpret. The coefficient matrix of the equations for the wheel/rail force is independent of the roughness and therefore this approach, combined with contact mechanics and wear process, can be used in the study of roughness growth and rail corrugation formation.

By assuming a smooth railhead, the response of the wheel/track system to the parametric excitation is obtained. Roughness equivalent to the parametric excitation is also defined. This equivalent roughness may, in addition to the actual rail roughness, be fed into the 'moving roughness models' and other previously developed models in which the parametric excitation has not been taken into account, so that the predictions from these models can be improved.

Results are presented firstly for a single locomotive wheel and then for four such wheels running over a conventional ballasted track at different speeds and excitation frequencies. At excitation frequencies much lower or higher than the pinned-pinned frequency of the track, the wheel speed has an insignificant effect on the response (magnitude) of the wheel/track system. Around the pinned-pinned frequency however, the role of the wheel speed cannot be neglected. Strong interactions between multiple wheels are also demonstrated, especially at frequencies above 600 Hz. The pinned-pinned effect and the interactions between the wheels combine together, making the response of the wheel/track system more sensitive to the wheel speed and to the positions of the wheels.

Dynamic wheel/rail forces due to the parametric excitation consist of mainly the first harmonic component at the sleeper-passing frequency if the wheel speed is low. However, at high wheel speeds, the second component at twice the sleeper-passing frequency can be as strong as the first. It is demonstrated that the equivalent roughness is more sensitive to the wheel speed and railpad stiffness at a wavelength equal to half the sleeper spacing. It must be noted that the sleeper-passing frequency is less than 150 Hz for current operational train speeds, and in this frequency range, the dynamics of the track bed, and sometimes even the ground, have significant contributions to the dynamic properties of the track [15]. In other words, to investigate responses to the parametric excitation, a more complete track model including the track bed and the supporting ground is needed.

Although a finite element formulation is presented in this report for the wheel dynamics, results are produced only for the rigid body wheel model. This allows the effect of the track on the wheel/rail interactions to be examined easily.

ACKOWLEDGEMENT

This work is supported by the EPSRC and Rail Research UK under project A3: *Railway noise: curve squeal, roughness growth, friction and wear.*

REFERENCES

[1] P. J. Remington 1987 *Journal of Acoustical Society of America*, **81**, 1805-1823. Wheel/rail rolling noise. Part I: Theoretical analysis.

[2] P. J. Remington 1987 *Journal of Acoustical Society of America*, **81**, 1824-1832. Wheel/rail rolling noise. Part II: Validation of the theory.

[3] D. J. Thompson, B. Hemsworth and N. Vincent 1996 *Journal of Sound and Vibration*, **193**, 123-135. Experimental validation of the TWINS prediction program for rolling noise. Part I: Description of the model and method.

[4] D. J. Thompson, P. Fodiman and H. Mahé 1996 *Journal of Sound and Vibration*, **193**, 137-147. Experimental validation of the TWINS prediction program for rolling noise. Part II: Results.

[5] S. Müller 1999 *Journal of Sound and Vibration* **227**(5), 899-913. A linear wheel-track model to predict instability and short pitch corrugation.

[6] K. Knothe 2000 *Rolling Contact Phenomena. CISME Courses and Lectures*, No. 411, 203-276, Springer, New York. Chapter 4 on non-steady state rolling contact and corrugations.

[7] A. Valdivia 1987 *PhD Dissertation, TU Berlin.* Interaction between high-frequency wheel-rail dynamics and irregular rail wear—a linear model.

[8] K. Hempelmann and K. Knothe 1996 *Wear* **191**, 161-169. An extended linear model for the prediction of short-pitch corrugation.

[9] C. O. Frederick 1986 *Proceedings of the Second Conference on the Contact Mechanics and Wear of Rail/Wheel Systems*, A rail corrugation theory.

[10] S. L. Grassie 2003 *Proceedings of the 6th International Conference on Contact Mechanics and Wear of Rail/Wheel Systems*, 11-19. Rail corrugation: advances in measurement, understanding and treatment.

[11] T. X. Wu and D. J. Thompson 2002 *Vehicle System Dynamics* **37** (3), 157-174. Behaviour of the normal contact force under multiple wheel/rail interactions.

[12] A. Nordborg 2002 *Journal of Acoustical Society of America* **111**(4), 1772-1781. Wheel/rail noise generation due to nonlinear effects and parametric excitation.

[13] X. Sheng, C. J. C. Jones and D. J. Thompson. Responses of infinite periodic structures to moving or stationary harmonic loads. Submitted to *Journal of Sound and Vibration.*

[14] D. J. Thompson 1993 *Journal of Sound and Vibration* **161**, 467-482. Wheel-rail noise generation, Part V: inclusion of wheel rotation.

[15] K. Knothe and Y. Wu 1999 *Structural Dynamics-EURODYN'99*, Balkema, Rotterdam, 849-853. Vertical substructual dynamics of vehicle-track-subgrade model.